PHYSICAL REVIEW B **81**, 195104 (2010)

Uranium 5*d*-5*f* electric-multipole transitions probed by nonresonant inelastic x-ray scattering

R. Caciuffo,[1] G. van der Laan,[2] L. Simonelli,[3] T. Vitova,[4] C. Mazzoli,[3] M. A. Denecke,[4] and G. H. Lander[1]
[1]*European Commission, Joint Research Centre, Institute for Transuranium Elements, Postfach 2340, D-76125 Karlsruhe, Germany*
[2]*Diamond Light Source, Chilton, Didcot OX11 0DE, United Kingdom*
[3]*European Synchrotron Radiation Facility, Boîte Postale 220 X, F-38043 Grenoble, France*
[4]*Karlsruhe Institute of Technology, Institut für Nukleare Entsorgung, P.O. Box 3640, D-76021 Karlsruhe, Germany*
(Received 31 December 2009; revised manuscript received 25 March 2010; published 5 May 2010)

Nonresonant inelastic x-ray scattering (NIXS) experiments have been performed to probe the 5d-5f electronic transitions at the uranium $O_{4,5}$ absorption edges in several systems characterized by either a localized or itinerant character of the U 5f electrons, namely, UO$_2$, USe, US, and elemental uranium in the α form. For small values of the scattering vector q, the spectra are dominated by dipole-allowed transitions encapsulated within the ill-defined giant resonance, whereas for higher values of q the multipolar transitions of rank $k=3$ and 5 give rise to strong and well-defined multiplet peaks in the pre-edge region. The origin of the observed nondipole multiplet structures is explained on the basis of many-electron atomic spectral calculations. The results obtained demonstrate the high potential of NIXS as a bulk-sensitive technique for the characterization of the electronic properties of actinide materials. The different U compounds show strong variations in the O_5 structure that can be correlated with the ground-state properties of the materials.

DOI: 10.1103/PhysRevB.81.195104 PACS number(s): 78.70.Ck, 71.10.−w

I. INTRODUCTION

Nonresonant inelastic x-ray scattering (NIXS) is emerging as a powerful bulk-sensitive probe of the dynamical electron-density response of solids and as a new tool for the investigation of the electronic structure in strongly correlated systems.[1–5] The sharp nondipolar prethreshold features that dominate the NIXS energy-loss spectrum at large momentum transfer[3] can be used to study atomic environment, valence, and hybridization effects[6] and give information on states with different symmetries to those of electric-dipole spectra obtained by x-ray absorption spectroscopy (XAS). No NIXS experiments have been performed so far on actinide solids, and the main aim of this work has been to explore the potential of NIXS for studying the nature of the 5f electron shell through the observation of multipole transitions from core 5d to valence 5f states. The actinide series is still only modestly understood. Several fundamental questions remain unanswered, including the number of electrons in valence states, the angular momentum coupling, and the character of the bonding. These factors have a huge influence in driving the peculiar magnetic and electronic properties of actinide metals,[7] alloys, and compounds.[8] The development of novel spectroscopic techniques sensitive to the ground-state properties of these systems is therefore of high importance.

Compared to resonant inelastic x-ray scattering (RIXS) and electron energy loss spectroscopy (EELS), the NIXS technique is penalized by a lower intensity, but it has the advantage that it permits a straightforward and quantitative interpretation of the spectra. Element specificity is provided by the energy positions of the core to valence transitions. Moreover, even when interrogating low-energy edges, NIXS remains a bulk-sensitive probe since the sampling depth is largely determined by the incident photon energy. The high-penetration depth of hard x-rays is also advantageous if the sample must be inside an outer container, e.g., if thermodynamical parameters such as temperature and pressure must be varied, or when the sample must be encapsulated for safety reasons.

Here we report the results of NIXS studies performed on single-crystal samples of UO$_2$, US, and USe, and on an epitaxial film of α uranium. NIXS spectra have been recorded at the uranium $O_{4,5}$ absorption edges, probing 5d-5f electronic multipole transitions.

UO$_2$ is a widely investigated semiconducting compound crystallizing in the fluorite structure and exhibiting long-range order of magnetic dipole and electric quadrupole moments at low temperature.[8,9] The U^{4+} ions are in the 5f^2 configuration with a $^3H_4$ ground state, with localized 5f states lying in the 5 eV gap between the O 2p band and the empty U 6d band, with a 5$f^2 \rightarrow 5f^1 6sd$ transition energy of 2–3 eV.[10] The valence, the ground-state symmetry, and the crystal field splitting are all well assessed on the basis of inelastic neutron scattering[11,12] and resonant x-ray diffraction[9] experiments.

The uranium monochalcogenides US and USe are examples of metallic compounds characterized by a narrow 5f band crossing the Fermi level and strongly hybridized with U 6d and 3p (US) or 4p (USe) states. These compounds have the NaCl cubic structure and exhibit a ferromagnetic ground state. The itinerant nature of the U 5f electrons in US has recently been confirmed by soft x ray photoemission spectroscopy studies.[13] In the case of USe, realistic electronic structure calculations based on the dynamical mean-field theory with a perturbative treatment of the effective quantum impurity problem have been reported.[14]

Metallic uranium exhibits an orthorhombic *Cmcm* structure (α-U) at room temperature, but below 43 K a charge-density-wave (CDW) modulation condenses from a soft phonon mode along the [100] direction.[15] Superconductivity is observed below 0.7 K in very high-quality single-crystal samples.[16] Uranium is indeed the only known element that features a CDW and superconductivity. Photoelectron energy distribution curves for polycrystalline samples show a giant

©2010 The American Physical Society

Fano-type resonance for the intensity of the $5f$ valence-band features at the Fermi energy E_F, when the photon energy is tuned through the $5d$ core absorption edge at around 94 to 103 eV.[17] The ground state properties of α-U are successfully described by first-principles calculations based on generalized gradient or local-density approximations of the density-functional theory, as the occupied band structure around the Fermi energy is not significantly affected by correlations.[18]

The outline of this paper is as follows. A more general theoretical introduction is given in Sec. II, describing what is precisely measured in the NIXS experiment. The details of the experiment are presented in Sec. III. The results of the measurements on the U compounds are presented in Sec. IV. In Sec. V, we describe the many-electron atomic spectral calculations which are used to interpret the experimental data. The results are discussed and analyzed in Sec. VI. The theoretical approach that we used is quantitatively appropriate in the case of strongly localized $5f$ electrons, as in UO_2, but gives qualitative information that is useful to understand the spectra also in the case of delocalized $5f$ electron states. A short summary and conclusions are found in Sec. VII.

II. GENERAL THEORY

In inelastic scattering, the cross section is measured as a function of the energy $\hbar\omega$ and momentum $\mathbf{q}$ transferred from the probe to the system. When the energy transfer is close to the binding energy of a core state, the inelastic scattering cross section strongly increases, which allows to study the core excitations of the system. In the low momentum transfer regime the scattering cross section is dominated by the dipole allowed excitations. The cross section is then proportional to the x-ray absorption coefficient and the direction $\mathbf{q}/|q|$ plays the role of the XAS polarization vector ϵ. As the magnitude of q increases, contributions from higher (dipole forbidden) excitations become important. The relative weights of the different excitation channels depend on the momentum transfer and the spatial extent of the wave functions.

The double differential cross section for NIXS can be expressed within the first Born approximation and is proportional to a dynamic structure factor $S(\mathbf{q},\omega)$ as

$$\frac{d^2\sigma}{d\Omega d\omega} = r_0^2\frac{\omega_f}{\omega_i}|\epsilon_i\cdot\epsilon_f^\star|^2 S(\mathbf{q},\omega), \tag{1}$$

where $\hbar\omega=\hbar\omega_i-\hbar\omega_f$ is the energy loss and $\mathbf{q}=\mathbf{k}_i-\mathbf{k}_f$ is the scattering vector, $\omega_{i,f}$, $\epsilon_{i,f}$, and $\mathbf{k}_{i,f}$ are the frequency, polarization, and wave vector, respectively, of the incident and scattered radiation. r_0 is the classical electron radius. The dynamic structure factor is related to the complex dielectric-response function $\varepsilon(\mathbf{q},\omega)$ by the fluctuation dissipation theorem,[19] $S(\mathbf{q},\omega)\propto q^2\Im[\varepsilon(\mathbf{q},\omega)^{-1}]$. In the following we will use the dynamic structure factor, which has the advantage that it contains no nonmaterial dependent factors.

The nonresonance radiation-matter interaction is dominated by a term proportional to the square of the vector potential $\mathbf{A}$ and according to Fermi's golden rule[4,6,20–22]

$$S(\mathbf{q},\omega) = \sum_f |\langle\psi_f|\mathrm{e}^{\mathrm{i}\mathbf{q}\cdot\mathbf{r}}|\psi_i\rangle|^2\delta(E_i-E_f+\hbar\omega), \tag{2}$$

where ψ_i and ψ_f are the total wave functions of the initial- and final-state configurations with energies E_i and E_f, respectively. The transition operator $\mathrm{e}^{\mathrm{i}\mathbf{q}\cdot\mathbf{r}}$ can be expanded in spherical multipoles,

$$\mathrm{e}^{\mathrm{i}\mathbf{q}\cdot\mathbf{r}} = \sum_{k=0}^{\infty}\sum_{m=-k}^{k}\mathrm{i}^k(2k+1)j_k(qr)C_m^{(k)*}(\theta_q,\phi_q)C_m^{(k)}(\theta_r,\phi_r), \tag{3}$$

where $j_k(qr)$ are spherical Bessel functions of rank k for the q-dependent radial component and $C_m^{(k)}(\theta,\phi) = \sqrt{4\pi/(2k+1)}Y_m^{(k)}(\theta,\phi)$ are normalized spherical harmonics. Assuming isotropic sample conditions, one can sum over m and interference terms vanish, Eq. (2) can then be cast in the form

$$S(\mathbf{q},\omega) = \sum_f\sum_{k=0}^{\infty} D_k|\langle\psi_f(r)|j_k(qr)|\psi_i(r)\rangle|^2\delta(E_i-E_f+\hbar\omega), \tag{4}$$

where the factors D_k are angular momentum coupling coefficients and the $\psi(r)$ are radial wave functions. Assuming the radial-matrix elements are constant over the spectral region of interest, $S(\mathbf{q},\omega)$ can be separated into an angular and a radial part. The angular part is a sum over the multipole contributions. The k-th term in this sum is equal to

$$I_k(\omega) \equiv \sum_f D_k\delta(E_i-E_f+\hbar\omega), \tag{5}$$

which depends on the initial state with energy E_i. The different multipole transitions excite the system to subsets of different symmetries and quantum numbers within the final state configuration. Details about the calculation of the angular integrated multipole spectra I_k, corresponding to the electric 2^k-pole transitions, are given in Sec. V A.

The multipole moments k for an $\ell\rightarrow\ell'$ shell transition are limited by the triangle condition, $|\ell-\ell'|\leq k\leq\ell+\ell'$, and the parity rule, $\ell+\ell'+k$=even. Thus for $d\rightarrow f$ transitions, only $k=1$ (dipole), $k=3$ (octupole), and $k=5$ (triakontadipole) transitions are allowed.

The radial part in Eq. (4) gives the weight factors of the I_k spectra in $S(\mathbf{q},\omega)$ as a function of q. The electric-dipole transition dominates the response of the system for low values of q, and with increasing q values the higher electric-multipole transitions become more important.

III. EXPERIMENTAL DETAILS

The experiment has been performed using the ID16 inverse geometry, multiple-analyzer-crystal spectrometer at the European Synchrotron Radiation Facility in Grenoble, France.[23] The beam generated by three consecutive undulators was monochromatized by a Si(111) double crystal, and horizontally focused by a Rh-coated mirror. The beam size at the sample position was 0.3×1.3 mm^2 (horizontal

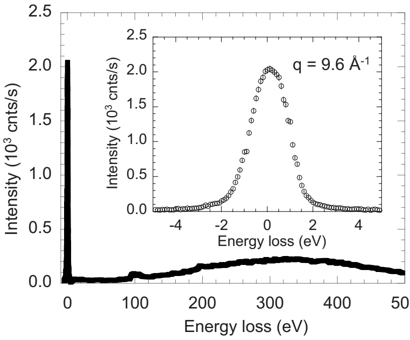

FIG. 1. Photon energy-loss spectrum measured for UO_2 at room temperature over an extended energy range including the elastic and Compton peaks. Data have been collected with a fixed final energy of 9.689 keV, at a transferred wave vector $q=9.6$ Å^{-1}. The inset shows the elastic peak, whose full width at half maximum is 1.3 eV.

× vertical). A set of nine spherically bent Si(660) analyzer crystals with 1 m bending radius, horizontal scattering geometry and vertical Rowland circles, provided a bandwidth of 1.3 eV at a final photon energy E_f of 9.689 keV, and an intensity of 7×10^{13} photons/s for a 25 μrad vertical divergence of the undulator radiation. The Bragg angle of the analyzers was fixed at 88.5°, and the geometry chosen in order to measure five different momentum-transfer values simultaneously, using a position sensitive detector based on a 256×256 photon counting pixel array. For these measurements we used a UO_2 single crystal with an external surface perpendicular to a [111] direction, US and USe crystals with natural faces perpendicular to (100), and a 2000 Å thick epitaxial film of α uranium, grown on a corundum (α-Al_2O_3) substrate and capped with a 50 Å thick Nb film. A He-flow cryo-cooler was used to cool the samples to a base temperature of 10 K. Data have been collected in symmetric reflection geometry by scanning the incident photon energy $\hbar\omega_i=\hbar\omega_f+\hbar\omega$ at fixed final energy, covering the $\hbar\omega$ energy-loss interval corresponding to the uranium $O_{4,5}$ ($5d\rightarrow5f$) absorption edges. In the case of the α-U thin film, a grazing-incidence geometry has been used to minimize the contribution of the corundum substrate to the measured signal.

Cross sections are particularly large between shells of the same principal quantum number, such as for the $5d\rightarrow5f$ transition. We also performed measurements across the uranium $N_{4,5}$ ($4d\rightarrow5f$) absorption edges, but failed to observe NIXS signals because the smaller radial overlap of initial and final wave functions results in a much lower cross section.

IV. EXPERIMENTAL RESULTS

Figure 1 shows a typical spectrum measured for UO_2 over an extended energy-loss range, keeping the scattering vector, q, fixed at a given value. The NIXS signal is obtained by fitting the broad Compton peak to a polynomial function and then subtracting it from the total measured intensity. The spectra obtained with this procedure for UO_2 at room temperature are shown in Fig. 2, where data at different q values are normalized to the peak intensity of the feature centered at about 104 eV.

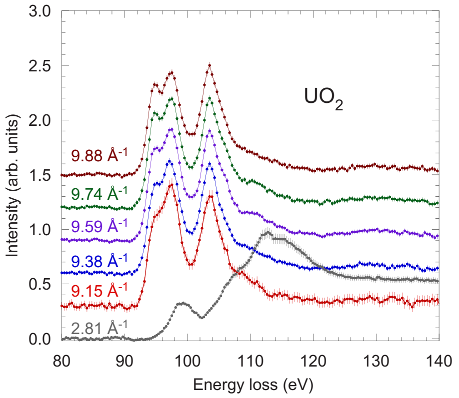

FIG. 2. (Color online) NIXS spectra measured for UO_2 at the uranium $O_{4,5}$ edges with a fixed final energy of 9.689 keV, at different values of the scattering vector q as indicated. The NIXS signal has been normalized to the peak centered at 104 eV in the high-q spectra.

The dipole spectrum, which is observed at $q=2.81$ Å^{-1}, shows the typical, ill-defined giant-resonance shape together with a prepeak around 99 eV, in good agreement with earlier XAS[24] and EELS[25,26] measurements. Increasing q above 9 Å^{-1}, the dipole transitions become negligible while pronounced peaks due to higher multipole transitions appear at lower energies. An asymmetric peak with a maximum at 103.6 eV and a clearly resolved double-peak feature with maxima at 94.9 and 97.3 eV characterize the spectrum at $q=9.88$ Å^{-1}. NIXS spectra for UO_2 have also been measured at 10 K, in the ordered antiferromagnetic-antiferroelectric quadrupole phase. A comparison with the room-temperature spectra does not reveal differences beyond the statistical error.

The NIXS spectra obtained at room temperature and $q=9.5$ Å^{-1} for the metallic systems US, USe, and α-U are shown in Fig. 3. The ground state and the electronic structure of the uranium monochalcogenides US and USe are very similar, and indeed the NIXS spectra observed for these two compounds are almost identical. For the feature at higher energy, the peak maximum is at 102.7 eV, about 1 eV lower than in UO_2. Moreover, the lower energy feature has not the double-peak shape observed in UO_2. In the α-U case, the NIXS response is similar to that of the monochalcogenides, the main difference being the relative intensity of the two features.

V. MANY-ELECTRON CALCULATIONS

A. Technicalities

Many-electron atomic spectral calculations enable us to identify the origin of the observed multipole transitions. These calculations are particularly powerful in the case of localized materials[7,27,28] and used here to calculate the electric-multipole transitions U $5f^2\rightarrow5d^95f^3$ for direct comparison with the measured spectra of UO_2.

The wave functions of the initial- and final-state configurations were calculated in intermediate coupling using Cowan's atomic Hartree-Fock (HF) code with relativistic

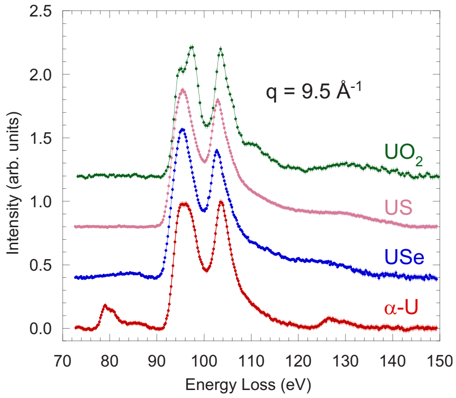

FIG. 3. (Color online) Experimental NIXS spectra measured at $q=9.5$ Å^{-1} for UO$_2$, US, USe, and α-U. The spectra are normalized to the peak intensity of the narrow feature near 104 eV and are shifted vertically by a constant amount. The features around 80 and 127 eV in the α-U spectrum are the Al $L_{2,3}$ signals from the α-Al$_2$O$_3$ substrate. Data on UO$_2$, US, and USe have been recorded in symmetric reflection geometry using single-crystal samples, whereas data on the α-U epitaxial film has been recorded in grazing incidence geometry.

corrections.[29] The obtained *ab initio* values of the Slater parameters, F^k and G^k, and the spin-orbit parameters, $\zeta(d)$ and $\zeta(f)$, are listed in Table I. For comparison, the values for the final-state configuration $4d^9 5f^3$, associated with the $N_{4,5}$ edge, are also displayed. The values show that the ratio $G^1(d,f)/\zeta(d)$, which determines the overall appearance of core level spectra,[30] increases from 0.05 for the $N_{4,5}$ edge to 3.9 for the $O_{4,5}$ edge. Hence, the electrostatic interactions, which produce a multiplet structure spread out over a wide energy range, govern in first instance the shape of the $O_{4,5}$ spectrum. However, as we will see in Sec. VI A, the interplay with the $5d$ spin-orbit interaction complicates the situation.

Angle-integrated electric 2^k-pole transitions have been calculated from the initial state U $5f^2$ to the final-state levels of the $5d^9 5f^3$ configuration in spherical symmetry, implicitly using the selection rules and symmetry constraints. In these calculations, the HF values of the Slater parameters were reduced with a scaling factor $g=0.7$ to account for screening effects. A scaling of typically $g=0.7$-0.8 is standard procedure in multiplet calculations for $3d$ transition metals,[31] rare earths,[27] and actinides[30,32] since it gives the best agreement with the measured core-level spectra. The calculated I_k spectra are shown in Fig. 4(b), where the intensities of the allowed transitions have been convoluted by a Lorentzian of half-width $\Gamma=0.5$ eV and a Gaussian of $\sigma=0.5$ eV.

TABLE I. Calculated Hartree-Fock values of the core-level energy, $E(d)$, Slater parameters, F^k and G^k, and spin-orbit parameters, ζ, for the initial- and final-state configurations in the transition $5f^2 \rightarrow nd^9 5f^3$. Parameter values for the $N_{4,5}$ edge are shown for comparison (all values in eV).

	U $5f^2$	$O_{4,5}$ $5d^9 5f^3$	$N_{4,5}$ $4d^9 5f^3$
$E(d)$		100.698	760.656
$F^2(f,f)$	9.514	9.711	9.970
$F^4(f,f)$	6.224	6.364	6.539
$F^6(f,f)$	4.569	4.677	4.807
$F^2(d,f)$		10.652	5.066
$F^4(d,f)$		6.850	2.033
$G^1(d,f)$		12.555	0.887
$G^3(d,f)$		7.768	0.957
$G^5(d,f)$		5.544	0.809
$\zeta(f)$	0.261	0.274	0.294
$\zeta(d)$		3.199	17.401

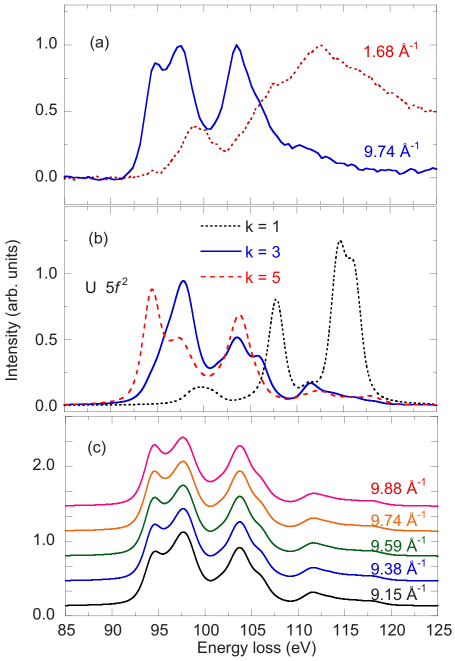

FIG. 4. (Color online) (a) Experimental NIXS spectra for UO$_2$ measured at 1.68 Å^{-1} (red dashed line) and 9.74 Å^{-1} (blue solid line) compared to results of atomic multiplet calculations for the U $5f^2$ configuration in (b). The I_k spectra, i.e., the calculated contributions to the cross section from dipole ($k=1$), octupole ($k=3$), and triakontadipole ($k=5$) transitions, are shown separately. The calculated spectra have been broadened by a Lorentzian of $\Gamma=0.5$ eV and Gaussian of $\sigma=0.5$ eV to match the experimental resolution. (c) Fits of the measured UO$_2$ spectra at different q values (from Fig. 2) using a linear combination of the calculated I_3 and I_5 spectra.

B. Dipole spectrum and giant resonance

Shallow core levels, such as the rare earth $N_{4,5}$ and actinide $O_{4,5}$ edges, show intense and broad structures known as giant or Fano resonances, which have been explained long ago.[33–36] In Fig. 2(a) the giant resonance appears in the measured dipole spectrum as a broad band around 112 eV with a weak shoulder at 108 eV. Figure 4(b) shows that the main dipole-allowed peaks lie within the energy region of the giant resonance of Fig. 4(a) ($q=1.68$ Å^{-1}). No broad features appear to be present in the higher multipole spectra, which are at lower energies. Also the prepeak in the dipole spectrum at $\sim$99 eV, which has previously been attributed to the finite spin-orbit interaction,[25,26] has a narrow line width. Convolution with a Lorentzian of half width $\Gamma \approx 4$ eV of the calculated transitions with energies above a threshold of 107 eV leads to a reasonable agreement with the measured giant resonance structure (result not shown).

The decay processes leading to the giant resonance can be included in the many-electron spectral calculation, although here we have not done so, because the problem is essentially solved. The strong Fano-resonance arises in the excitation-decay process $5f^n+\hbar\omega \rightarrow 5d^9 5f^{n+1} \leftrightarrow 5d^{10}5f^{n-1}\varepsilon\ell$ in resonance with the direct excitation $5f^n+\hbar\omega \rightarrow 5d^{10}5f^{n-1}\varepsilon\ell$ due to the large radial matrix element $R(5d,\varepsilon\ell;5f,5f)$ of the super-Coster-Kronig decay, where $\varepsilon\ell$ represents a continuum state. Many-electron spectral calculations have been presented previously for the Gd $4d \rightarrow 4f$ giant resonance[37] and the Pu $5d \rightarrow 5f$ giant resonance.[38] These calculations gave a good agreement with the experiment for the energy shifts and line widths of all the transition both above and below the onset of the giant resonance.

C. Higher multipole contributions

The calculated spectra I_k for $k=1$, 3, and 5 are presented in Fig. 4(b). Each spectrum has the same integrated intensity equal to $(14-n)(2J+1)/(2\ell+1)=108/7$, which is determined by the number of f holes and the level multiplicity in the ground state.[29] The relative weights of the I_k contributions in the NIXS spectrum is determined by the radial parts of the wave functions and changes gradually as a function of q. Using the atomic wave functions of U the maxima of the $k=1$, 3, and 5 contributions are around $q=3$ Å^{-1}, 7 Å^{-1}, and 9 Å^{-1}, respectively. Therefore, at $q=2.81$ Å^{-1} only dipole transitions play a role, whereas these are very small above $q=9$ Å^{-1}. Going from $q=9.15$ to 9.88 Å^{-1}, the experimental data in Fig. 2 show that the $k=5$ contribution increases with respect to the $k=3$. We fitted these UO$_2$ spectra measured at the different q values using a linear combination of the calculated I_3 and I_5 spectra. Assuming a linear behavior in this q range, the fit gives the I_5/I_3 ratio as ~0.79 and ~1.27 at $q=9.15$ and 9.88 Å^{-1}, respectively.

The fitted theoretical spectra, displayed in Fig. 4(c), show a good agreement with the measured spectra in Fig. 2. They reflect the main characteristics of the NIXS spectra, namely that with increasing q in the doublet structure the low-energy peak (at ~95) increases in intensity relative to the high-energy peak (~97 eV). Concurrently, the asymmetric peak (at ~104 eV) increases in relative intensity, confirming that it contains two different k contributions.

VI. DISCUSSION

A. Characteristics of the spectral structure

The higher-order transitions show a spectacular shift to lower energy of more than 10 eV compared to the dipole transitions. This pulls the final states below the onset of the giant resonance resulting in an increase in the lifetime and hence a sharp multiplet structure. Similar results have recently been reported in the case of the rare-earths $N_{4,5}$ edge for Ce compounds.[6] In order to explain such large differences between the different multipole spectra we need to delve into the details of the selection rules and the interplay between electrostatic and spin-orbit interactions. We will denote the spin, orbital, and total angular momenta as S,L,J and S',L',J' for the initial- and final-state configuration, respectively. In the NIXS process, the final-state J' and L' values are restricted by the triangle conditions $|J-k| \leq J' \leq J+k$ and $|L-k| \leq L'+\Delta S \leq L+k$, respectively, where $\Delta S=0$ in LS coupling and $\Delta S=\pm 1$ in intermediate coupling. Thus, for initial state $5f^2$ $^3H_4$, dipole transitions are allowed to final states ^3G, ^3H, ^3I with $J'=3,4,5$, where in intermediate coupling quintet-spin states can mix in by $5d$ core spin-orbit interaction. The selection rules have implications for the final states that can be reached. For the transitions $f^n \rightarrow d^9 f^{n+1}$ with less than half-filled shell, the maximum spin in the initial state is one less than in the final state. Since electric-multipole transitions obey the selection rule $\Delta S=0$, the high-spin final state is a *ghost* state, which cannot be reached from the initial state without spin-orbit interaction.[31] A similar situation arises for L' and J'. While the f^2 ground state has $L=5$ and $J=4$, the final state d^9f^3 contains values up to $L'=8$ and $J'=7$. High L' and J' values cannot be reached by dipole transitions, only by higher multipole transitions.

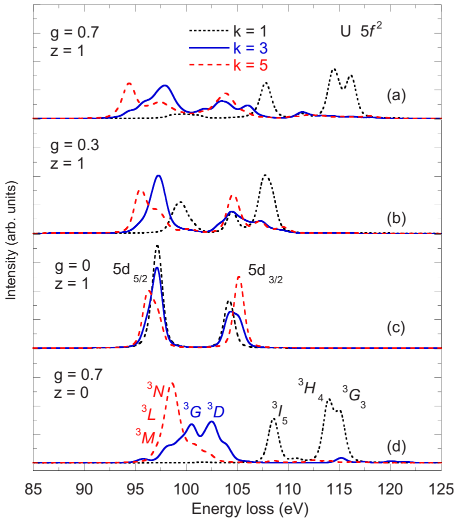

FIG. 5. (Color online) Calculated multipole spectra with $k=1$ (black dotted line), $k=3$ (blue solid line), and $k=5$ (red dashed line) for the transition U $5f^2 \rightarrow 5d^9 5f^3$ varying the scaling factors g for the Slater parameters and z for the spin-orbit parameters. (a) Realistic values: $g=0.7$, $z=1$ (intermediate coupling scheme applies), (b) strongly reduced electrostatic interactions: $g=0.3$, $z=1$, (c) only spin-orbit interaction, $z=1$ (jj-coupling limit), and (d) only electrostatic interactions, $g=0.7$ (LS-coupling limit). The approximate peak assignment is indicated when meaningful. Since states are strongly mixed in intermediate coupling peak assignment is less meaningful. Calculated spectra have been convoluted with a Lorentzian of $\Gamma=0.2$ eV and Gaussian of $\sigma=0.4$ eV.

Next, we must consider the energy distribution of the allowed final states. In Fig. 5(a) we have redrawn the multipole spectra from Fig. 4(b) using slightly narrower line widths ($\Gamma=0.2$ eV, $\sigma=0.4$ eV). In panels (b)–(d) the spectra are calculated with different scaling factors g for the Slater parameters and z for the spin-orbit parameter. While panel

(a) shows the spectra for realistic values ($g=0.7, z=1$), (b) shows the spectra with strongly reduced electrostatic interactions ($g=0.3, z=1$), (c) with only spin-orbit interaction (jj-coupling scheme applies), and (d) with only electrostatic interactions (LS-coupling scheme applies). In the last case the approximate peak assignment is indicated when meaningful, however none of the levels is pure, and a peak assignment in the intermediate coupling case is hardly meaningful, as the states are strongly mixed.

The electrostatic interactions give a large energy spread over the different $L'S'$ states of about 30 eV. As a rule, states with higher S' and L' values have lower energies; however, it must be stressed that the second Hund's rule is not strictly valid in the final state so that states with intermediate L' value can have a lower energy.[31] Figure 5(d) shows that in LS coupling, i.e., in the presence of only electrostatic interactions, the dipole-allowed final states ($k=1$) have much higher energies than the other states. The reason is that if the momentum transfer q in the excitation process is small, the charge cloud in the final state has to be oriented in approximately the same way as in the initial state, which results in a high electrostatic energy. In strong contrast, the higher multipole transitions allow final states where the angular distribution of the charge density is more evenly spread, thereby reducing the electrostatic energy.

In LS coupling [Fig. 5(d)], the spin of all final states is the same as the initial state, i.e., $S'=S=3$. When the $L'S'$ states are mixed by spin-orbit interaction they acquire roughly speaking an energy separation of

$$\Delta E \approx \sqrt{(\Delta_{\text{electrostatic}})^2 + (\Delta_{\text{spin-orbit}})^2}.$$

For instance, in the case of the dipole-allowed spectrum ($k=1$)with triplet spin, located at higher energies, the spin-orbit coupling switches on the prepeak at ~99 eV with quintet-spin character.[25] Comparison of Figs. 5(a) and 5(b), where the scaling has been reduced from $g=0.7$ to 0.3, shows that in the dipole spectrum the peak position, as well as prepeak intensity, is most sensitive to scaling of the electrostatic interactions. On the other hand, the higher multipole allowed $L'S'$ states are closely bundled together and for this reason they experience a strong spin-orbit interaction. Consequently, these states will split into two structures with an energy separation slightly exceeding $\Delta_{\text{spin-orbit}}=\frac{5}{2}\zeta(5d) \approx 8$ eV. The result is a set of states grouped at low energy containing a $5d_{5/2}$ core hole and a set of states grouped at high energy containing a $5d_{3/2}$ core hole [see Fig. 5(c)]. Thus, despite the large electrostatic interaction, the core hole spin-orbit interaction manifests itself prominently, causing the main energy splitting in the higher multipole spectra. Therefore, the two main features in the NIXS spectrum at ~95 and ~104 eV can be assigned to O_5 ($5d_{5/2}\rightarrow 5f$) and O_4 ($5d_{3/2}\rightarrow 5f$), respectively.

B. Spectra of different U compounds

It is possible to transfer the general analysis in Sec. VI A the spectra of the other U systems shown in Fig. 3. These materials have quite different electronic structures. UO_2 has a $5f^2$ ground state, US and USe are closer to $5f^3$, and α-U shows an itinerant $5f$ behavior. Many-electron calculations show that going from f^2 to f^3 the shapes of the I_3 and I_5 spectra do not change very much, in contrast to the I_1 spectrum. The peak separation of the I_5 peak at 95 eV and I_3 peak at 97 eV, making up the doublet in the NIXS spectra, is a bit smaller for f^3 than for f^2 (results not shown).

The high-q spectra of the U compounds in Fig. 3 show a splitting of 8–9 eV, which can be ascribed to the $5d$ spin-orbit interaction. All compounds exhibit a similar O_4 peak (at ~104 eV) but have a distinctly different O_5 peak (at ~95 eV), which is caused by the electrostatic interactions. Hence, while all U systems share the splitting by the spin-orbit interaction, they can be distinguished by the variations observed in the O_5 structure, which can be related to the specific ground-state properties such as the angular-momentum composition.

The electronic screening and electron (de)localization of the $5f$ electrons can also play an important role. Since the intensity maxima of the I_5 and I_3 contributions in the O_5 peak differ in energy by ~2 eV, the spectral shape depends strongly on the relative weight of these two multipole contributions. This is not the case for the O_4 peak, where both contributions practically coincide in energy. For a given q value, the relative contributions of the different multipoles in the NIXS spectrum depend on the extension of the $5f$ wave function. A certain multipole has optimal intensity if the spherical Bessel function of the same order has a period comparable to the size of the local $5f$ orbital. This means that if the $5f$ orbitals become more delocalized, the weight of higher multipoles increases. Thus a larger $k=5$ contribution can explain the spectral shape of α-U, US, and USe Admittedly, many-electron atomic calculations work well for localized systems but are less applicable to delocalized materials. Additional calculations such as using the local density approximation and the dynamical mean field theory (LDA+DMFT) (Ref. 39) would be beneficial to better understand the variations in the NIXS spectra between the U compounds. However, it is already clear that NIXS at the $O_{4,5}$ edges offers great potential since this technique is able to reveal the strong variations among the uranium compounds. We have demonstrated that the structure within the O_5 peak can be correlated with the ground-state properties of the materials. In contrast to the $N_{4,5}$ and $M_{4,5}$ absorption spectra,[7,24,30,40] which show little or no structure within the spin-orbit split core levels, the $O_{4,5}$ edges show a distinct structure caused by the electrostatic interactions between core and valence electrons. Since electric-multipole transitions from the ground state reach only a limited subset of final states, they provide a fingerprint for the specific ground state.

VII. CONCLUSIONS

In conclusion, we have demonstrated the high potential of the NIXS technique for studying bulk actinide compounds. The intrinsic intensity limitation of the technique can be overcome by using an optimized spectrometer at a third-generation synchrotron-radiation source. The instrumental energy resolution allows us to resolve details of the multiplet structure. For the localized $5f$ electrons in UO_2 a good agreement is obtained with many-electron spectral calculations in intermediate coupling, where as usual the Hartree-Fock values of the Slater integrals are reduced to 70%. The electric-multipole transitions from the ground state can reach only a limited subset of final states, thereby providing a fingerprint for the specific ground state. We have shown that a high momentum transfer leads to $k=3$ and $k=5$ multipole transitions with final states of high-angular momentum, which are shifted to lower energy by more than 10 eV. These transitions are well below the onset of the giant resonance and therefore have a narrow line width. The peak splitting of 8–9 eV observed in all the NIXS spectra can be ascribed to the core hole $5d$ spin-orbit interaction, allowing a peak assignment of O_5 and O_4. This energy splitting perseveres in covalent and delocalized U compounds. The material-dependent spectral structure of the O_5 peak shows a clear correlation with the nature of the ground state. These results are very promising for perusing further NIXS measurements in a wide range of investigations on transuranium materials, with a focus on the dual localized-delocalized nature of the $5f$ electrons and their instability induced by external pressure.

ACKNOWLEDGMENTS

We thank Roger Ward of Oxford University for the loan of the epitaxial uranium sample, P. Colomp and the ESRF radioprotection staff for assistance in handling the uranium samples, and the ID16 technical staff for assistance during the experiment.

---

[1] A. T. Macrander, P. A. Montano, D. L. Price, V. I. Kushnir, R. C. Blasdell, C. C. Kao, and B. R. Cooper, Phys. Rev. B **54**, 305 (1996).

[2] I. G. Gurtubay, J. M. Pitarke, W. Ku, A. G. Eguiluz, B. C. Larson, J. Tischler, P. Zschack, and K. D. Finkelstein, Phys. Rev. B **72**, 125117 (2005).

[3] B. C. Larson, J. Z. Tischler, W. Ku, C.-C. Lee, O. D. Restrepo, A. G. Eguiluz, P. Zschack, and K. D. Finkelstein, Phys. Rev. Lett. **99**, 026401 (2007).

[4] M. W. Haverkort, A. Tanaka, L. H. Tjeng, and G. A. Sawatzky, Phys. Rev. Lett. **99**, 257401 (2007).

[5] M. van Veenendaal and M. W. Haverkort, Phys. Rev. B **77**, 224107 (2008).

[6] R. A. Gordon, G. T. Seidler, T. T. Fister, M. W. Haverkort, G. A. Sawatzky, A. Tanaka, and T. K. Sham, EPL **81**, 26004 (2008).

[7] K. T. Moore and G. van der Laan, Rev. Mod. Phys. **81**, 235 (2009).

[8] P. Santini, S. Carretta, G. Amoretti, R. Caciuffo, N. Magnani, and G. H. Lander, Rev. Mod. Phys. **81**, 807 (2009).

[9] S. B. Wilkins, R. Caciuffo, C. Detlefs, J. Rebizant, E. Colineau, F. Wastin, and G. H. Lander, Phys. Rev. B **73**, 060406(R) (2006).

[10] Y. Baer and J. Schönes, Solid State Commun. **33**, 885 (1980).

[11] R. Caciuffo, G. Amoretti, P. Santini, G. H. Lander, J. Kulda, and P. de V. Du Plessis, Phys. Rev. B **59**, 13892 (1999).

[12] E. Blackburn, R. Caciuffo, N. Magnani, P. Santini, P. J. Brown, M. Enderle, and G. H. Lander, Phys. Rev. B **72**, 184411 (2005).

[13] Y. Takeda, T. Okane, T. Ohkochi, Y. Saitoh, H. Yamagami, A. Fujimori, and A. Ochiai, Phys. Rev. B **80**, 161101(R) (2009).

[14] L. V. Pourovskii, M. I. Katsnelson, and A. I. Lichtenstein, Phys. Rev. B **72**, 115106 (2005).

[15] G. H. Lander, E. S. Fisher, and S. D. Bader, Adv. Phys. **43**, 1 (1994).

[16] J. L. O'Brien *et al.*, Phys. Rev. B **66**, 064523 (2002).

[17] M. Iwan, E. E. Koch, and F.-J. Himpsel, Phys. Rev. B **24**, 613 (1981).

[18] A. N. Chantis, R. C. Albers, M. D. Jones, M. van Schilfgaarde, and T. Kotani, Phys. Rev. B **78**, 081101(R) (2008).

[19] P. Nozières and D. Pines, Phys. Rev. **113**, 1254 (1959).

[20] W. Schülke, H. Nagasawa, S. Mourikis, and P. Lanzki, Phys. Rev. B **33**, 6744 (1986).

[21] M. Blume, J. Appl. Phys. **57**, 3615 (1985).

[22] J. A. Soininen, A. L. Ankudinov, and J. J. Rehr, Phys. Rev. B **72**, 045136 (2005).

[23] R. Verbeni, T. Pylkkänen, S. Huotari, L. Simonelli, G. Vankó, K. Martel, C. Henriquet, and G. Monaco, J. Synchrotron Radiat. **16**, 469 (2009).

[24] G. Kalkowski, G. Kaindl, W. D. Brewer, and W. Krone, Phys. Rev. B **35**, 2667 (1987).

[25] K. T. Moore and G. van der Laan, Ultramicroscopy **107**, 1201 (2007).

[26] M. T. Butterfield, K. T. Moore, G. van der Laan, M. A. Wall, and R. G. Haire, Phys. Rev. B **77**, 113109 (2008).

[27] B. T. Thole, G. van der Laan, J. C. Fuggle, G. A. Sawatzky, R. C. Karnatak, and J. M. Esteva, Phys. Rev. B **32**, 5107 (1985).

[28] G. van der Laan, Lect. Notes Phys. **697**, 143 (2006).

[29] R. D. Cowan, *The Theory of Atomic Structure and Spectra* (University of California Press, Berkeley, CA, 1981).

[30] G. van der Laan, K. T. Moore, J. G. Tobin, B. W. Chung, M. A. Wall, and A. J. Schwartz, Phys. Rev. Lett. **93**, 097401 (2004).

[31] B. T. Thole and G. van der Laan, Phys. Rev. B **38**, 3158 (1988).

[32] J. H. Shim, K. Haule, and G. Kotliar, EPL **85**, 17007 (2009).

[33] J. L. Dehmer, A. F. Starace, U. Fano, J. Sugar, and J. W. Cooper, Phys. Rev. Lett. **26**, 1521 (1971).

[34] A. F. Starace, Phys. Rev. B **5**, 1773 (1972).

[35] J. Sugar, Phys. Rev. B **5**, 1785 (1972).

[36] *Giant Resonances in Atoms, Molecules and Solids*, NATO Advanced Study Institute Series B: Physics, edited by J. P. Connerade, J. M. Esteva, and R. C. Karnatak (Plenum Press, New York, 1987), Vol. 151.

[37] K. Starke, E. Navas, E. Arenholz, Z. Hu, L. Baumgarten, G. van der Laan, C. T. Chen, and G. Kaindl, Phys. Rev. B **55**, 2672 (1997).

[38] J. Terry, R. K. Schulze, J. D. Farr, T. Zocco, K. Heinzelman, E. Rotenberg, D. K. Shuh, G. van der Laan, D. A. Arena, and J. G. Tobin, Surf. Sci. **499**, L141 (2002).

[39] J. H. Shim, K. Haule, and G. Kotliar, Nature (London) **446**, 513 (2007).

[40] S. P. Collins, D. Laundy, C. C. Tang, and G. van der Laan, J. Phys.: Condens. Matter **7**, 9325 (1995).